

Back-Projection based Fidelity Term for Ill-Posed Linear Inverse Problems

Tom Tirer, and Raja Giryes

Abstract—Ill-posed linear inverse problems appear in many image processing applications, such as deblurring, super-resolution and compressed sensing. Many restoration strategies involve minimizing a cost function, which is composed of fidelity and prior terms, balanced by a regularization parameter. While a vast amount of research has been focused on different prior models, the fidelity term is almost always chosen to be the least squares (LS) objective, that encourages fitting the linearly transformed optimization variable to the observations. In this work, we examine a different fidelity term, which has been implicitly used by the recently proposed iterative denoising and backward projections (IDBP) framework. This term encourages agreement between the projection of the optimization variable onto the row space of the linear operator and the pseudo-inverse of the linear operator (“back-projection”) applied on the observations. We analytically examine the difference between the two fidelity terms for Tikhonov regularization and identify cases where the new term has an advantage over the standard LS one. Moreover, we demonstrate empirically that the behavior of the two induced cost functions for sophisticated convex and non-convex priors, such as total-variation, BM3D, and deep generative models, correlates with the obtained theoretical analysis.

Index Terms—Inverse problems, image restoration, image deblurring, image super-resolution, compressed sensing, total variation, non-convex priors, BM3D, deep generative models.

I. INTRODUCTION

Inverse problems appear in many fields of science and engineering, where the goal is to recover a signal from its observations that are obtained by some acquisition process. In image processing, the observations are usually a degraded version of the latent image, which may be noisy, blurred, downsampled, or all together. Such observation models, and others, can be formulated by a linear model

$$\mathbf{y} = \mathbf{A}\mathbf{x} + \mathbf{e}, \quad (1)$$

where $\mathbf{x} \in \mathbb{R}^n$ represents the unknown original image, $\mathbf{y} \in \mathbb{R}^m$ represents the observations, \mathbf{A} is an $m \times n$ degradation matrix (sometimes also referred to as the measurement matrix) and $\mathbf{e} \in \mathbb{R}^m$ is a noise vector. For example, this model corresponds to the problem of denoising [1]–[4] when \mathbf{A} is the $n \times n$ identity matrix \mathbf{I}_n ; inpainting [5]–[7] when \mathbf{A} is an $m \times n$ sampling matrix (i.e. a selection of m rows of \mathbf{I}_n); deblurring [8], [9] when \mathbf{A} is a blur operator; super-resolution [10], [11] if \mathbf{A} is a composite operator of blurring (e.g. anti-aliasing filtering) and down-sampling; and compressed sensing when \mathbf{A} is a (random) measurement matrix ($m \ll n$) and the

signal is sparse under some basis representation [12]–[14] or resides in a general union of low-dimensional subspaces [15], [16].

The inverse problems represented by (1) are usually ill-posed, i.e. the measurements do not suffice for obtaining a successful reconstruction. Therefore, a vast amount of research has focused on designing good prior models for natural images. In fact, many of the methods for the problems mentioned above differ only in their prior assumptions and not in the way that they enforce fidelity to the observations.

To be more formal, a common strategy for recovering \mathbf{x} aims at minimizing a cost function of the form

$$f(\tilde{\mathbf{x}}) = \ell(\tilde{\mathbf{x}}) + \beta s(\tilde{\mathbf{x}}), \quad (2)$$

where $\ell(\tilde{\mathbf{x}})$ is a fidelity term, $s(\tilde{\mathbf{x}})$ is a prior term (can be also referred to as the regularizer), β is a positive scalar that controls the level of regularization, and $\tilde{\mathbf{x}}$ is the optimization variable. Many different prior functions are used in the literature, whether explicitly, e.g. total-variation (TV) [1], or implicitly, e.g. BM3D [4] and deep generative models [17]. Yet, most of the works use a typical least squares (LS) fidelity term

$$\ell_{LS}(\tilde{\mathbf{x}}) \triangleq \frac{1}{2} \|\mathbf{y} - \mathbf{A}\tilde{\mathbf{x}}\|_2^2, \quad (3)$$

where $\|\cdot\|_2$ stands for the Euclidean norm. This term can be also derived from the negative log-likelihood function, under the assumption that the noise \mathbf{e} is a vector of i.i.d. Gaussian random variables $e_i \sim \mathcal{N}(0, \sigma_e^2)$.

In this work, we examine a different fidelity term, which has been implicitly used by the recently proposed iterative denoising and backward projections (IDBP) framework [18] (we elaborate on this method in Section II-B). Under the practical assumptions that $m \leq n$ and $\text{rank}(\mathbf{A}) = m$, we examine the fidelity term

$$\ell_{BP}(\tilde{\mathbf{x}}) \triangleq \frac{1}{2} \|\mathbf{A}^\dagger \mathbf{y} - \mathbf{A}^\dagger \mathbf{A}\tilde{\mathbf{x}}\|_2^2, \quad (4)$$

where $\mathbf{A}^\dagger \triangleq \mathbf{A}^T(\mathbf{A}\mathbf{A}^T)^{-1}$ is the pseudoinverse of the full row-rank matrix \mathbf{A} . Note that $\mathbf{P}_A \triangleq \mathbf{A}^\dagger \mathbf{A}$ is an orthogonal projection onto the row space of \mathbf{A} , and that \mathbf{A}^\dagger can be interpreted as a “back-projection” (BP) from $\mathbb{A}\mathbb{R}^n$ back to \mathbb{R}^n . Therefore, the fidelity (4) encourages agreement between $\mathbf{P}_A \tilde{\mathbf{x}}$ —the projection of $\tilde{\mathbf{x}}$ onto the row space of \mathbf{A} , and $\mathbf{A}^\dagger \mathbf{y}$ —the back-projection of the measurements. In general, this is different than $\ell_{LS}(\tilde{\mathbf{x}})$ that encourages agreement between $\mathbf{A}\tilde{\mathbf{x}}$ and \mathbf{y} . Note that in the noiseless case, i.e. when $\mathbf{y} = \mathbf{A}\mathbf{x}$, the terms in (3) and (4) are translated to fitting $\mathbf{A}\tilde{\mathbf{x}}$ to $\mathbf{A}\mathbf{x}$ and $\mathbf{P}_A \tilde{\mathbf{x}}$ to $\mathbf{P}_A \mathbf{x}$, respectively.

This work was supported by the European research council (ERC starting grant 757497 PI Giryes). The authors are with the School of Electrical Engineering, Tel Aviv University, Tel Aviv 69978, Israel. (email: tirer.tom@gmail.com, raja@tauex.tau.ac.il)

Note that for some inverse problems $\ell_{LS}(\tilde{\mathbf{x}})$ and $\ell_{BP}(\tilde{\mathbf{x}})$ may coincide. For example, in image inpainting, where \mathbf{A} is a selection of m rows of \mathbf{I}_n , we have that $\mathbf{A}^\dagger = \mathbf{A}^T$ is an $n \times m$ matrix that merely pads with $n - m$ zeros the vector on which it is applied, and so $\|\mathbf{A}^\dagger(\mathbf{y} - \mathbf{A}\tilde{\mathbf{x}})\|_2^2 = \|\mathbf{y} - \mathbf{A}\tilde{\mathbf{x}}\|_2^2$. Therefore, we specifically focus on three popular inverse problems: super-resolution, deblurring and certain compressed sensing scenarios, where the two fidelity terms, $\ell_{LS}(\tilde{\mathbf{x}})$ and $\ell_{BP}(\tilde{\mathbf{x}})$, are indeed very different.

Contribution. This work makes a first attempt towards characterizing for which observation model \mathbf{A} and prior $s(\tilde{\mathbf{x}})$ it is better to use each of the following objectives:

$$f_{LS}(\tilde{\mathbf{x}}) \triangleq \frac{1}{2} \|\mathbf{y} - \mathbf{A}\tilde{\mathbf{x}}\|_2^2 + \beta s(\tilde{\mathbf{x}}), \quad (5)$$

$$f_{BP}(\tilde{\mathbf{x}}) \triangleq \frac{1}{2} \|\mathbf{A}^\dagger \mathbf{y} - \mathbf{A}^\dagger \mathbf{A}\tilde{\mathbf{x}}\|_2^2 + \beta s(\tilde{\mathbf{x}}). \quad (6)$$

Particularly, for $s(\tilde{\mathbf{x}})$ being the Tikhonov regularization (the ℓ_2 prior), where closed-form solutions exist, we derive analytical expressions for the estimations' mean square error (MSE) that allow to examine which fidelity term is preferable. For example, we show that in the noiseless case $f_{BP}(\tilde{\mathbf{x}})$ yields provably better restoration than $f_{LS}(\tilde{\mathbf{x}})$, for any given value of β , if the singular values of \mathbf{A} are smaller than 1 (e.g. in typical super-resolution problems).

For sophisticated convex and non-convex priors, such as TV [1], BM3D [4], and DCGAN [19], analytical analysis is intractable. Therefore, we perform an intensive empirical study, where we use the same optimization method (FISTA [20] or ADAM [21]) to minimize each of the two different cost functions. Interestingly, we demonstrate that the behavior for the sophisticated priors strongly correlates with properties for which we establish concrete mathematical reasoning in the case of ℓ_2 priors.

The paper is organized as follows. In Section II we briefly describe the IDBP framework, and show that differently to the way it is developed in [18], it is essentially the proximal gradient method [20], [22] (popularized under the name ISTA) applied on $f_{BP}(\tilde{\mathbf{x}})$. Section III includes mathematical analysis of the two cost functions for the case of ℓ_2 -type priors. The analytical results are verified in Section IV. In Section V the two cost functions are empirically examined for different sophisticated priors. Section VI concludes the paper.

II. THE IDBP FRAMEWORK

A. Background

The iterative denoising and backward projections (IDBP) framework [18] is inspired by the plug-and-play priors concept [23], which encourages the usage of existing Gaussian denoisers as "black boxes" to implicitly dictate the prior $s(\tilde{\mathbf{x}})$ when solving inverse problems. Such an approach allows one to use sophisticated denoising methods even when it is not clear how to formulate their associated priors, e.g. convolutional neural network (CNN) denoisers.

Several plug-and-play works have been published [23]–[31]. Most of them consider the typical cost function (5) and directly minimize it using existing iterative optimization schemes, such as FISTA [20], ADMM [32] or quadratic penalty method [33],

that include steps in which the proximal mapping of $s(\tilde{\mathbf{x}})$ is used (as explained below, this mapping is equivalent to Gaussian denoising under the prior $s(\tilde{\mathbf{x}})$).

Recently, [18] has suggested, after several manipulations, to solve a different optimization problem

$$\min_{\tilde{\mathbf{x}}, \tilde{\mathbf{z}}} \frac{1}{2(\sigma_e + \delta)^2} \|\tilde{\mathbf{z}} - \tilde{\mathbf{x}}\|_2^2 + s(\tilde{\mathbf{x}}) \quad \text{s.t.} \quad \mathbf{A}\tilde{\mathbf{z}} = \mathbf{y}, \quad (7)$$

where σ_e is the noise level and δ is a design parameter. This work has also proposed an adaptive strategy to set δ , which does not depend on the prior and, contrary to cross-validation, does not require a set of ground truth examples. It has been suggested in [18] to solve (7) using a simple alternating minimization scheme that possesses the plug-and-play property, where the prior term $s(\tilde{\mathbf{x}})$ is handled solely by a Gaussian denoising operation $\mathcal{D}(\cdot; \sigma)$ with noise level $\sigma = \sigma_e + \delta$. In this iterative method, $\tilde{\mathbf{z}}_k$ is obtained by projecting $\tilde{\mathbf{x}}_{k-1}$ onto $\{\mathbf{A}\mathbb{R}^n = \mathbf{y}\}$

$$\begin{aligned} \tilde{\mathbf{z}}_k &= \underset{\tilde{\mathbf{z}}}{\operatorname{argmin}} \|\tilde{\mathbf{z}} - \tilde{\mathbf{x}}_{k-1}\|_2^2 \quad \text{s.t.} \quad \mathbf{A}\tilde{\mathbf{z}} = \mathbf{y} \\ &= \mathbf{A}^\dagger \mathbf{y} + (\mathbf{I}_n - \mathbf{A}^\dagger \mathbf{A})\tilde{\mathbf{x}}_{k-1} \\ &= \tilde{\mathbf{x}}_{k-1} + \mathbf{A}^\dagger(\mathbf{y} - \mathbf{A}\tilde{\mathbf{x}}_{k-1}). \end{aligned} \quad (8)$$

and $\tilde{\mathbf{x}}_k$ is obtained by

$$\begin{aligned} \tilde{\mathbf{x}}_k &= \underset{\tilde{\mathbf{x}}}{\operatorname{argmin}} \frac{1}{2(\sigma_e + \delta)^2} \|\tilde{\mathbf{z}}_k - \tilde{\mathbf{x}}\|_2^2 + s(\tilde{\mathbf{x}}) \\ &\triangleq \mathcal{D}(\tilde{\mathbf{z}}_k; \sigma_e + \delta). \end{aligned} \quad (9)$$

The two repeating operations lends the method its name: Iterative Denoising and Backward Projections (IDBP). After a stopping criterion is met, the last $\tilde{\mathbf{x}}_k$ is taken as the estimate of the latent \mathbf{x} . Note that in many cases the operation \mathbf{A}^\dagger can be performed efficiently (e.g. the matrix inversion can be avoided using the conjugate gradient method [34]), and thus IDBP is dominated by the complexity of the denoising operation, similarly to other plug-and-play techniques. Using sophisticated denoisers, such as BM3D and CNNs, this algorithm has achieved excellent results for deblurring [18], [35] and super-resolution [36].

B. Obtaining IDBP by applying ISTA on $f_{BP}(\tilde{\mathbf{x}})$

Interestingly, there is another way to develop the exact algorithm, which is different from the way it is developed in [18]. First, note that (7) can be solved directly for $\tilde{\mathbf{z}}$. Similar to (8), we get

$$\tilde{\mathbf{z}}^* = \mathbf{A}^\dagger \mathbf{y} + (\mathbf{I}_n - \mathbf{A}^\dagger \mathbf{A})\tilde{\mathbf{x}}. \quad (10)$$

Substituting (10) into (7), we reach $\min_{\tilde{\mathbf{x}}} f_{BP}(\tilde{\mathbf{x}})$ with a specific value of the regularization parameter, i.e. $\beta = (\sigma_e + \delta)^2$. Therefore, IDBP is essentially a specific method to minimize the $f_{BP}(\tilde{\mathbf{x}})$ cost function. Let us show that this method coincides with applying the proximal gradient method [20], [22], popularized under the name ISTA¹, on $f_{BP}(\tilde{\mathbf{x}})$. Let us define the proximal mapping, which was introduced by

¹ISTA is the abbreviation of Iterative Shrinkage-Thresholding Algorithm, initially designed for $s(\tilde{\mathbf{x}}) = \|\tilde{\mathbf{x}}\|_1$ [37].

Moreau [38] for convex functions, though, here we do not limit this definition to convex functions.

Definition 1. *The proximal mapping of a function $s(\cdot)$ at the point \tilde{z} is defined by*

$$\text{prox}_{s(\cdot)}(\tilde{z}) \triangleq \underset{\tilde{x}}{\text{argmin}} \frac{1}{2} \|\tilde{z} - \tilde{x}\|_2^2 + s(\tilde{x}). \quad (11)$$

Clearly, given the same $s(\cdot)$, Gaussian denoising and proximal mapping are tightly connected $\mathcal{D}(\tilde{z}; \sigma) = \text{prox}_{\sigma^2 s(\cdot)}(\tilde{z})$.

Assuming a differentiable fidelity term $\ell(\tilde{x})$ with a Lipschitz continuous gradient $\nabla\ell(\tilde{x})$, applying ISTA on (2) involves iterations of

$$\tilde{x}_k = \text{prox}_{\mu\beta s(\cdot)}(\tilde{x}_{k-1} - \mu\nabla\ell(\tilde{x}_{k-1})), \quad (12)$$

where μ is a step-size, which ensures convergence for convex $s(\cdot)$ if it is smaller than 1 over the Lipschitz constant of $\nabla\ell(\tilde{x})$ [20].

Proposition 1. *The IDBP algorithm, given in (8) and (9), coincides with applying ISTA (12) on the cost function $f_{BP}(\tilde{x})$.*

Proof. Let us compute $\nabla\ell_{BP}(\tilde{x})$. Using the properties $\mathbf{P}_A \triangleq \mathbf{A}^\dagger \mathbf{A} = \mathbf{P}_A^T = \mathbf{P}_A^2$ and $\mathbf{P}_A \mathbf{A}^\dagger = \mathbf{A}^\dagger$, we get

$$\begin{aligned} \nabla\ell_{BP}(\tilde{x}) &= -\mathbf{P}_A(\mathbf{A}^\dagger \mathbf{y} - \mathbf{P}_A \tilde{x}) \\ &= -\mathbf{A}^\dagger(\mathbf{y} - \mathbf{A}\tilde{x}). \end{aligned} \quad (13)$$

The Lipschitz constant of $\nabla\ell_{BP}(\tilde{x})$ can be computed as the spectral norm of the Hessian $\nabla^2\ell_{BP}(\tilde{x})$. Therefore, μ can be chosen as

$$\mu = \frac{1}{\|\nabla^2\ell_{BP}(\tilde{x})\|} = \frac{1}{\|\mathbf{P}_A\|} = 1, \quad (14)$$

where we use the fact that the spectral norm of a non-trivial orthogonal projection is 1. Now, due to the connection $\mathcal{D}(\tilde{z}; \sigma) = \text{prox}_{\sigma^2 s(\cdot)}(\tilde{z})$, (12) can be written as

$$\tilde{x}_k = \mathcal{D}(\tilde{x}_{k-1} - \mu\nabla\ell(\tilde{x}_{k-1}); \sqrt{\mu\beta}). \quad (15)$$

Finally, by plugging (13) and (14) into (15) and setting $\beta = (\sigma_e + \delta)^2$, we get the IDBP scheme, which is presented in (8) and (9). \square

The connection between IDBP and ISTA, allows IDBP to adopt the theoretical results of the latter [20]. Yet, note that the powerful global convergence (obtaining the optimal value of the objective) of ISTA holds only for denoisers that are associated with convex prior functions. This limitation is shared also with ADMM-based plug-and-play schemes [24].

III. MATHEMATICAL ANALYSIS FOR ℓ_2 PRIORS

In this section, we turn to analyze the performance of the new cost function and compare it to (5). We consider a type of ℓ_2 prior functions, for which the closed-form solutions of (5) and (6) lead to a tractable performance analysis. We start with specifying the required assumptions, then we derive the estimators and expressions for their expected mean square error. Finally, the error expressions are compared and several observations are stated.

A. Assumptions

In order to allow a concrete mathematical comparison between $f_{BP}(\tilde{x})$ and $f_{LS}(\tilde{x})$, in the theoretical analysis we restrict our discussion to ℓ_2 prior functions of the form $s(\tilde{x}) = \|\mathbf{D}\tilde{x}\|_2^2$, where $\mathbf{D}^T \mathbf{D}$ is a positive-definite matrix. This prior is often referred to as Tikhonov regularization and is one of the most widely used methods to solve ill-posed inverse problems. Yet, for obtaining analytical results, we further focus on a more specific type of this prior—we require that both \mathbf{A} and \mathbf{D} have the same right singular vectors. Let us define the singular value decomposition (SVD) of the $m \times n$ matrix $\mathbf{A} = \mathbf{U}\mathbf{\Lambda}\mathbf{V}^T$, where \mathbf{U} is an $m \times m$ orthogonal matrix whose columns are the left singular vectors, $\mathbf{\Lambda}$ is an $m \times n$ rectangular diagonal matrix with nonzero singular values $\{\lambda_i\}_{i=1}^m$ on the diagonal, and \mathbf{V} is an $n \times n$ orthogonal matrix whose columns are the right singular vectors. The property that $\{\lambda_i\}_{i=1}^m$ are strictly positive follows from our assumptions in Section I, that $m \leq n$ and $\text{rank}(\mathbf{A}) = m$. For \mathbf{D} , essentially, we assume that $\mathbf{D}^T \mathbf{D} = \mathbf{V}\mathbf{\Gamma}^2\mathbf{V}^T \succ 0$, where $\mathbf{\Gamma}^2$ is an $n \times n$ diagonal matrix of nonzero eigenvalues $\{\gamma_i^2\}_{i=1}^n$.

The assumption above is required because, as far as we know, currently there is no known analytical expression for the eigen-decomposition of arbitrary matrices $\mathbf{A}^T \mathbf{A} + \mathbf{D}^T \mathbf{D}$ which is required for our analysis [39]. Yet, this assumption holds in some practical cases, e.g. if \mathbf{A} and \mathbf{D} are circulant matrices (and thus diagonalized by the discrete Fourier transform), or if $\mathbf{D} = \mathbf{I}_n$ (i.e. least-norm regularization).

B. Performance analysis

Let us start with obtaining closed-form expressions for the estimators \hat{x}_{LS} and \hat{x}_{BP} , which minimize $f_{LS}(\tilde{x})$ and $f_{BP}(\tilde{x})$, respectively. Due to the convexity of the cost functions, this is done simply by equating their gradients to zero

$$\begin{aligned} \nabla f_{LS}(\tilde{x}) &= -\mathbf{A}^T(\mathbf{y} - \mathbf{A}\tilde{x}) + \beta\mathbf{D}^T \mathbf{D}\tilde{x} = \mathbf{0} \\ &\Rightarrow \hat{x}_{LS} = (\mathbf{A}^T \mathbf{A} + \beta\mathbf{D}^T \mathbf{D})^{-1} \mathbf{A}^T \mathbf{y}, \end{aligned} \quad (16)$$

$$\begin{aligned} \nabla f_{BP}(\tilde{x}) &= -\mathbf{P}_A(\mathbf{A}^\dagger \mathbf{y} - \mathbf{P}_A \tilde{x}) + \beta\mathbf{D}^T \mathbf{D}\tilde{x} = \mathbf{0} \\ &\Rightarrow \hat{x}_{BP} = (\mathbf{P}_A + \beta\mathbf{D}^T \mathbf{D})^{-1} \mathbf{A}^\dagger \mathbf{y}. \end{aligned} \quad (17)$$

We turn to compute the expected mean square errors (MSEs) of the estimators under the assumptions that $\mathbb{E}[e] = \mathbf{0}$ and $\mathbb{E}[ee^T] = \sigma_e^2 \mathbf{I}_m$. To ease formulations, we define the $n - m$ zero eigenvalues of $\mathbf{A}^T \mathbf{A}$ (i.e. zeros in the diagonal of $\mathbf{\Lambda}^T \mathbf{\Lambda}$) by $\{\lambda_i^2\}_{i=m+1}^n$.

The computation of the MSE of \hat{x}_{LS} is given by

$$\begin{aligned} MSE_{LS} &= \mathbb{E}\|\hat{x}_{LS} - \mathbf{x}\|_2^2 \\ &= \mathbb{E}\|(\mathbf{A}^T \mathbf{A} + \beta\mathbf{D}^T \mathbf{D})^{-1} \mathbf{A}^T (\mathbf{A}\mathbf{x} + e) - \mathbf{x}\|_2^2 \\ &= \mathbb{E}\|((\mathbf{A}^T \mathbf{A} + \beta\mathbf{D}^T \mathbf{D})^{-1} \mathbf{A}^T \mathbf{A} - \mathbf{I}_n) \mathbf{x}\|_2^2 \\ &\quad + \sigma_e^2 \text{Tr}((\mathbf{A}^T \mathbf{A} + \beta\mathbf{D}^T \mathbf{D})^{-2} \mathbf{A}^T \mathbf{A}) \\ &= \mathbb{E}\|\mathbf{V}((\mathbf{\Lambda}^T \mathbf{\Lambda} + \beta\mathbf{\Gamma}^2)^{-1} \mathbf{\Lambda}^T \mathbf{\Lambda} - \mathbf{I}_n) \mathbf{V}^T \mathbf{x}\|_2^2 \\ &\quad + \sigma_e^2 \text{Tr}(\mathbf{V}(\mathbf{\Lambda}^T \mathbf{\Lambda} + \beta\mathbf{\Gamma}^2)^{-2} \mathbf{\Lambda}^T \mathbf{\Lambda} \mathbf{V}^T) \\ &= \sum_{i=1}^n \left(\frac{\lambda_i^2}{\lambda_i^2 + \beta\gamma_i^2} - 1 \right)^2 [\mathbf{V}^T \mathbf{x}]_i^2 + \sigma_e^2 \sum_{i=1}^n \frac{\lambda_i^2}{(\lambda_i^2 + \beta\gamma_i^2)^2}. \end{aligned} \quad (18)$$

The second equality follows from substituting (1) in (16), the third equality uses the assumptions on the expected value and covariance of \mathbf{e} , and the cyclic property of trace, the fourth equality is obtained by substituting the eigen-decompositions of $\mathbf{A}^T \mathbf{A}$ and $\mathbf{D}^T \mathbf{D}$, and the last equality follows from the fact that \mathbf{V} is an orthogonal matrix. Therefore, by defining the (squared) bias and variance terms as

$$\begin{aligned} bias_{LS}^2 &\triangleq \sum_{i=1}^m \underbrace{\left(\frac{\beta \gamma_i^2}{\lambda_i^2 + \beta \gamma_i^2} \right)^2}_{\triangleq bias_{LS}^{2(i)}} [\mathbf{V}^T \mathbf{x}]_i^2 + \sum_{i=m+1}^n [\mathbf{V}^T \mathbf{x}]_i^2, \\ var_{LS} &\triangleq \sum_{i=1}^m \underbrace{\frac{\sigma_e^2}{\lambda_i^2 (1 + \beta \gamma_i^2 / \lambda_i^2)}}_{\triangleq var_{LS}^{(i)}}, \end{aligned} \quad (19)$$

we may write the error as

$$MSE_{LS} = bias_{LS}^2 + var_{LS}. \quad (20)$$

Note that the bias depends on the original image \mathbf{x} and not on the noise, and the opposite holds for the variance. Yet, both terms are affected by the structure of \mathbf{A} . The regularization parameters $\beta, \{\gamma_i\}$ introduce a tradeoff: increasing them reduces the variance but increases the bias.

To ease the computation of the MSE of $\hat{\mathbf{x}}_{BP}$, let us also define an indicator function $1_{i \leq m}$ that is equal to 1 if $i \leq m$ and 0 otherwise, and an $n \times n$ diagonal matrix $\mathbf{I}_{i \leq m}$ with $\{1_{i \leq m}\}_{i=1}^n$ on its diagonal. The following identities are used

$$\begin{aligned} \mathbf{P}_A &= \mathbf{V} \mathbf{I}_{i \leq m} \mathbf{V}^T, \\ \mathbf{A}^\dagger &= \mathbf{V} \mathbf{\Lambda}^T (\mathbf{\Lambda} \mathbf{\Lambda}^T)^{-1} \mathbf{U}^T, \\ \mathbf{A}^\dagger \mathbf{A}^{\dagger T} &= \mathbf{V} \mathbf{\Lambda}^T (\mathbf{\Lambda} \mathbf{\Lambda}^T)^{-2} \mathbf{\Lambda} \mathbf{V}^T. \end{aligned} \quad (21)$$

Now, we get

$$\begin{aligned} MSE_{BP} &= \mathbb{E} \|\hat{\mathbf{x}}_{BP} - \mathbf{x}\|_2^2 \\ &= \mathbb{E} \left\| (\mathbf{P}_A + \beta \mathbf{D}^T \mathbf{D})^{-1} \mathbf{A}^\dagger (\mathbf{A} \mathbf{x} + \mathbf{e}) - \mathbf{x} \right\|_2^2 \\ &= \left\| ((\mathbf{P}_A + \beta \mathbf{D}^T \mathbf{D})^{-1} \mathbf{P}_A - \mathbf{I}_n) \mathbf{x} \right\|_2^2 \\ &\quad + \sigma_e^2 \text{Tr} \left((\mathbf{P}_A + \beta \mathbf{D}^T \mathbf{D})^{-2} \mathbf{A}^\dagger \mathbf{A}^{\dagger T} \right) \\ &= \left\| \mathbf{V} \left((\mathbf{I}_{i \leq m} + \beta \mathbf{\Gamma}^2)^{-1} \mathbf{I}_{i \leq m} - \mathbf{I}_n \right) \mathbf{V}^T \mathbf{x} \right\|_2^2 \\ &\quad + \sigma_e^2 \text{Tr} \left(\mathbf{V} (\mathbf{I}_{i \leq m} + \beta \mathbf{\Gamma}^2)^{-2} \mathbf{\Lambda}^T (\mathbf{\Lambda} \mathbf{\Lambda}^T)^{-2} \mathbf{\Lambda} \mathbf{V}^T \right) \\ &= \sum_{i=1}^n \left(\frac{1_{i \leq m}}{1_{i \leq m} + \beta \gamma_i^2} - 1 \right)^2 [\mathbf{V}^T \mathbf{x}]_i^2 + \sigma_e^2 \sum_{i=1}^n \frac{\lambda_i^{-2} 1_{i \leq m}}{(1_{i \leq m} + \beta \gamma_i^2)^2}. \end{aligned} \quad (22)$$

The second equality follows from substituting (1) in (17), the third equality uses the assumptions on \mathbf{e} and the cyclic property of trace, the fourth equality is obtained by substituting the eigen-decompositions of \mathbf{P}_A , $\mathbf{D}^T \mathbf{D}$ and $\mathbf{A}^\dagger \mathbf{A}^{\dagger T}$, and

the last equality uses the orthogonality of \mathbf{V} . Therefore, by defining

$$\begin{aligned} bias_{BP}^2 &\triangleq \sum_{i=1}^m \underbrace{\left(\frac{\beta \gamma_i^2}{1 + \beta \gamma_i^2} \right)^2}_{\triangleq bias_{BP}^{2(i)}} [\mathbf{V}^T \mathbf{x}]_i^2 + \sum_{i=m+1}^n [\mathbf{V}^T \mathbf{x}]_i^2, \\ var_{BP} &\triangleq \sum_{i=1}^m \underbrace{\frac{\sigma_e^2}{\lambda_i^2 (1 + \beta \gamma_i^2)}}_{\triangleq var_{BP}^{(i)}}, \end{aligned} \quad (23)$$

we have that

$$MSE_{BP} = bias_{BP}^2 + var_{BP}. \quad (24)$$

Comparing (19) and (23) we may notice the following. First, the term $bias_{BP}^2$ handles small $\{\lambda_i\}_{i=1}^m$ (i.e. singular values of \mathbf{A} that are smaller than 1) better than $bias_{LS}^2$. However, var_{BP} handles such small singular values worse than var_{LS} . The opposite holds for singular values that are greater than 1. This behavior can be formulated as the following observation.

Observation 1. For $\lambda_i < 1$ we have that $bias_{BP}^{2(i)} < bias_{LS}^{2(i)}$ but $var_{BP}^{(i)} > var_{LS}^{(i)}$. And, for $\lambda_i > 1$ we have that $bias_{BP}^{2(i)} > bias_{LS}^{2(i)}$ but $var_{BP}^{(i)} < var_{LS}^{(i)}$.

Notice that in the noiseless case $\sigma_e = 0$, implying that $MSE_{LS} = bias_{LS}^2$ and $MSE_{BP} = bias_{BP}^2$. This leads us to the following observation for the noiseless case.

Observation 2. In a noiseless scenario, the relation between $\sum_{i=1}^m bias_{BP}^{2(i)}$ and $\sum_{i=1}^m bias_{LS}^{2(i)}$, dictates the relation between MSE_{BP} and MSE_{LS} . In particular, if all the singular values of \mathbf{A} are smaller than 1, then $MSE_{BP} < MSE_{LS}$, and if all the singular values of \mathbf{A} are greater than 1, then $MSE_{BP} > MSE_{LS}$.

Note that Observation 2 holds for any given setting of β that is used by the two estimators. Therefore, these relations between MSE_{BP} and MSE_{LS} hold also when β is tuned for best performance of each estimator. Notice that in the 'in particular'-part in Observation 2, if all the singular values are much smaller (or larger) than 1 then $bias_{BP}^{2(i)}$ is much smaller (or larger) than $bias_{LS}^{2(i)}$ for every i . In such cases, the gap between $bias_{LS}^2$ and $bias_{BP}^2$ may be substantial enough to dictate the relationship between the MSEs also in the high SNR case, where MSE_{LS} and MSE_{BP} are approximately equal to the bias terms.

As can be seen in (19) and (23), for the discussed Tikhonov regularization the bias term of each estimator is minimized if $\beta \rightarrow 0$, and in this case $bias_{LS}^2$ tends to $bias_{BP}^2$. This means that the performance gap in the noiseless case, which is stated in Observation 2, tends to zero for $\beta \rightarrow 0$. However, note that we consider here ℓ_2 priors mainly as a surrogate to complex priors which are hard to analyze. As we demonstrate in Section V, the results that are obtained for sophisticated priors, such as TV, BM3D and DCGAN, indeed strongly correlate with the observations above. For such priors, the optimal value of β for each fidelity term is significantly above 0 even in the

noiseless case (contrary to ℓ_2 priors), and the gap between the best recoveries is significant as well.

An important factor that is not taken into account in the above analysis is optimization, since for ℓ_2 priors there is a closed-form solution. Yet, for sophisticated priors iterative optimization schemes are inevitable, and the regularization parameter has an effect which is similar to the step size in these schemes. In such cases, extremely low value of β inherently results in a massive slowdown in the convergence for convex priors [40], [41] and/or bad local minima for non-convex priors. Taking a numerical optimization point of view, in the sequel we empirically show that $\hat{\mathbf{x}}_{BP}$ is superior to $\hat{\mathbf{x}}_{LS}$ even for ℓ_2 priors with $\beta \rightarrow 0$, if few iterations of conjugate gradients are used instead of the closed-form expressions (16) and (17). This implementation choice may be preferable in high-dimensional problems when it is not possible to invert the matrices. The advantage of BP in this case follows from the fact that the eigenvalues of \mathbf{P}_A are only 1 (in the row space of \mathbf{A}) and 0 (in the null space of \mathbf{A}), while $\mathbf{A}^T \mathbf{A}$ may have very different eigenvalues in general, and conjugate gradients (among other methods) performs better when the eigenvalues are clustered [42].

IV. EXPERIMENTS WITH ℓ_2 PRIORS

In this section, we discuss the implications of the analytical results from Section III and verify them for specific observation models: super-resolution and compressed sensing. In the first, all the singular values of \mathbf{A} are smaller than 1, while in the latter it is possible that all of them are greater than 1. We also discuss the typical deblurring problem, where all the singular values of \mathbf{A} are smaller than 1 (except one that equals 1). In this case, \mathbf{A}^\dagger in $\hat{\mathbf{x}}_{BP}$ has to be regularized due to the large number of near zero singular values, and (22) needs to be modified accordingly.

A. Super-resolution

Let us consider the super-resolution (SR) task, where \mathbf{A} is a composite operator of blurring (e.g. anti-aliasing filtering) followed by down-sampling. Note that the largest singular value of a typical filtering operation is 1, and it is associated with the DC. The rest of the singular values are smaller than 1. The subsequent operator is subsampling, which inevitability reduces the energy of the signal (as $m < n$). Therefore, essentially, all the singular values of \mathbf{A} are smaller than 1. This property is demonstrated in Fig. 1a for SR with scale factor 3 and Gaussian filter of size 7×7 and standard deviation 1.6 (used in many works, e.g. [11], [29], [36]), which is performed on a 64×64 image (thus $n = 4096$ and $m = 484$). We consider such a small image to allow computing the SVD of \mathbf{A} (our analytic expressions require both $\{\lambda_i^2\}_{i=1}^m$ and \mathbf{V}).

We verify our analytical results for the SRx3 scenario mentioned above, and two cases: $\sigma_e = 0$ and Gaussian noise with $\sigma_e = \sqrt{2}$. The experiments are performed on the *cameraman* image, resized to 64×64 pixels. In the noisy case, we average the results over 5 noise realizations. We have observed similar results for other images as well. We use the ℓ_2

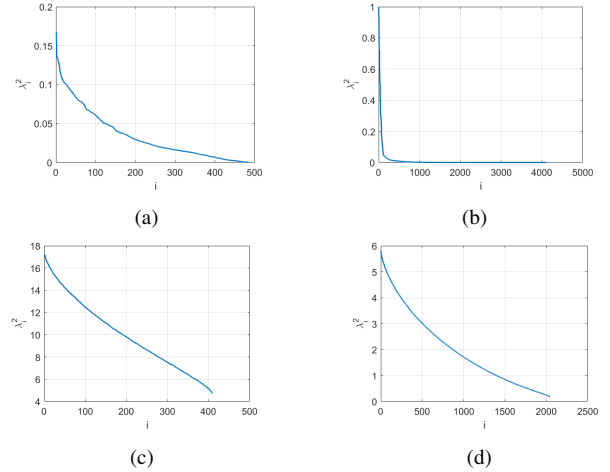


Fig. 1: The (squared) singular values of \mathbf{A} applied on a 64×64 image for: (a) SRx3 with 7×7 Gaussian filter; (b) blurring with 9×9 uniform filter; (c) CS with $m = 0.1n$ Gaussian measurements and Haar basis; (d) CS with $m = 0.5n$ Gaussian measurements and Haar basis.

prior $s(\tilde{\mathbf{x}}) = \|\tilde{\mathbf{x}}\|_2^2$, which satisfies the assumptions ($\mathbf{D} = \mathbf{I}_n$ and $\gamma_i = 1$).

The PSNR² results are presented in Fig. 2 and validate the analytical expressions. For $\sigma_e = 0$, $\hat{\mathbf{x}}_{BP}$ is better than $\hat{\mathbf{x}}_{LS}$ for any value of the parameter β , as implied by Observation 2 since all the singular values of \mathbf{A} are smaller than 1 (Fig. 1a). For $\sigma_e = \sqrt{2}$, the gap between the estimators is reduced because var_{BP} is worse than var_{LS} at handling the small singular values, as mentioned in Observation 1.

To demonstrate the numerical optimization advantage of the BP cost over the LS cost for $\beta \rightarrow 0$ (where the gap between the bias terms in (19) and (23) tends to 0), we repeat the experiments above for very small values of β . However, this time instead of inverting the matrices in (16) and (17) we obtain the estimators using the conjugate gradient method. The results are presented in Fig. 3. Remarkably, a single iteration is enough for obtaining the exact BP estimator (for ℓ_2 prior).

B. Compressed sensing

Contrary to SR scenarios, in compressed sensing (CS) the singular values of \mathbf{A} may be larger than 1. Consider the commonly examined scenario where \mathbf{A} is the multiplication of an $m \times n$ Gaussian measurement matrix (whose i.i.d. entries are drawn from $\mathcal{N}(0, 1/m)$) with an $n \times n$ Haar wavelet basis. We have observed that for high compression, e.g. $m/n = 0.1$, all the singular values are larger than 1, as demonstrated in Fig. 1c. However, for lower compression, e.g. $m/n = 0.5$, there are also singular values smaller than 1, as demonstrated in Fig. 1d.

We verify our analytical results for these two compression ratios (both with $\sigma_e = 0$). The experiments are performed on the same 64×64 version of *cameraman* image, and we use again the ℓ_2 prior $s(\tilde{\mathbf{x}}) = \|\tilde{\mathbf{x}}\|_2^2$. The results are presented in

²The PSNR for a recovery $\hat{\mathbf{x}}$ of a uint8 image $\mathbf{x} \in \mathbb{R}^n$ is computed as $10 \log_{10} \left(\frac{255^2}{\frac{1}{n} \|\hat{\mathbf{x}} - \mathbf{x}\|_2^2} \right)$.

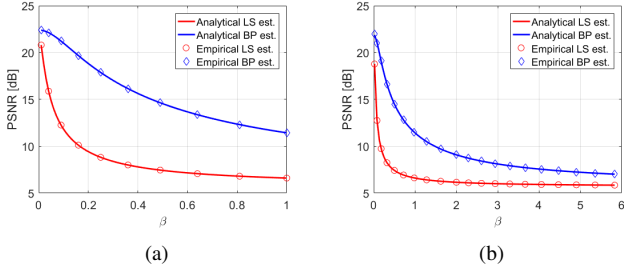


Fig. 2: Super-resolution with Gaussian filter and scale factor of 3, using ℓ_2 prior. PSNR (for *cameraman*) vs. β (regularization parameter), for (a) $\sigma_e = 0$, and (b) $\sigma_e = \sqrt{2}$.

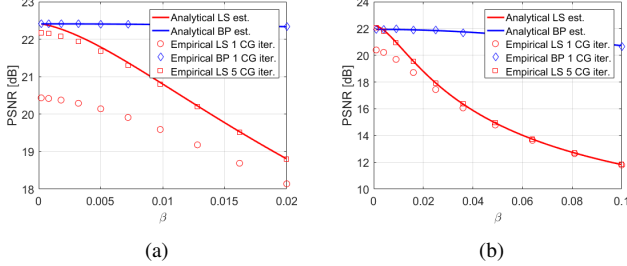


Fig. 3: Super-resolution with Gaussian filter and scale factor of 3, using ℓ_2 prior and iterations of conjugate gradients instead of matrix inversion. PSNR (for *cameraman*) vs. β (regularization parameter), for (a) $\sigma_e = 0$, and (b) $\sigma_e = \sqrt{2}$.

Fig. 4 and validate the analytical expressions. For $m/n = 0.1$, \hat{x}_{LS} is better than \hat{x}_{BP} for any value of β , as implied by Observation 2 since all the singular values of \mathbf{A} are greater than 1 (Fig. 1c). Interestingly, for $m/n = 0.5$, where some singular values of \mathbf{A} are smaller than 1 (Fig. 1d), \hat{x}_{BP} gets better results than \hat{x}_{LS} .

We demonstrate again the numerical optimization advantage of the BP cost over the LS cost by repeating the experiments above for very small values of β , while using the conjugate gradient method instead of matrix inversion. The results are presented in Fig. 5. It can be seen again that for the ℓ_2 prior a single iteration is enough for obtaining the exact BP estimator.

We find it necessary to emphasize that compressed sensing scenarios require a sparsity-inducing prior, e.g. $s(\tilde{\mathbf{x}}) = \|\tilde{\mathbf{x}}\|_1$, rather than an ℓ_2 prior, for which both estimators exhibit poor results (i.e. very low PSNR). However, our purpose here is merely to validate our analysis, which applies only to ℓ_2 priors, and show that when all (or many) singular values are greater than 1, \hat{x}_{LS} might be better than \hat{x}_{BP} .

Finally, note that for Gaussian \mathbf{A} there is no efficient way to implement the operators \mathbf{A} and \mathbf{A}^T for large dimensions. Therefore, in practice, taking \mathbf{A} to be the subsampled Fourier transform is more common, e.g. in sparse MRI [43]. However, note that for this acquisition model \mathbf{A}^\dagger is simply the Hermitian transpose of \mathbf{A} (this property follows from the fact that the subsampled Fourier transform is a tight frame [44]), which together with the unitarity of the Fourier transform leads to $\|\mathbf{A}^\dagger(\mathbf{y} - \mathbf{A}\tilde{\mathbf{x}})\|_2^2 = \|\mathbf{y} - \mathbf{A}\tilde{\mathbf{x}}\|_2^2$. This means that the two cost functions coincide, which is also implied by the fact that in this case all the singular values of \mathbf{A} are 1 and thus (18) is

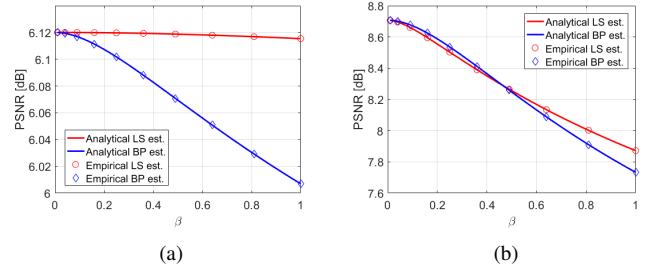


Fig. 4: Compressed sensing with Gaussian measurements and Haar basis, using ℓ_2 prior. PSNR (for *cameraman*) vs. β (regularization parameter), for (a) $m = 0.1n$, and (b) $m = 0.5n$.

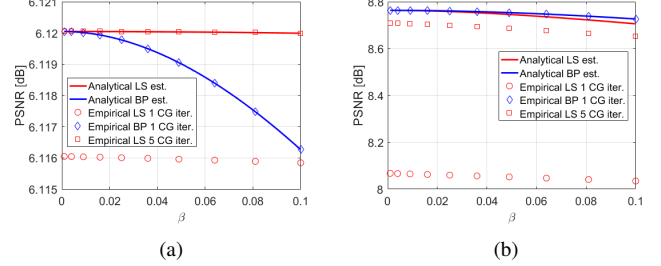


Fig. 5: Compressed sensing with Gaussian measurements and Haar basis, using ℓ_2 prior and iterations of conjugate gradients instead of matrix inversion. PSNR (for *cameraman*) vs. β (regularization parameter), for (a) $m = 0.1n$, and (b) $m = 0.5n$.

identical to (22). Therefore, we do not make a comparison for this case.

C. Deblurring

In the deblurring problem, \mathbf{A} is a square ($m = n$) ill-conditioned matrix that performs blurring (i.e. filtering by a blur kernel). Typically, the blur kernel coefficients are normalized such that their sum is 1. Thus, the largest singular value of \mathbf{A} is 1 (associated with the DC), and many other singular values are near 0. This is demonstrated in Fig. 1b for uniform kernel of size 9×9 (used in many works, e.g. [8], [9], [18]).

Note that if one uses \hat{x}_{BP} , exactly as defined in (17), Observation 2 implies an advantage of \hat{x}_{BP} over \hat{x}_{LS} in the noiseless case due to better handling the small singular values in the bias term. However, since in the deblurring problem \mathbf{A} is not rank-deficient but rather (very) ill-conditioned, deblurring scenarios always assume that the measurements are noisy (typically with low noise levels). Therefore, it is required to regularize the inversion of $\mathbf{A}\mathbf{A}^T$ in \mathbf{A}^\dagger in order to mitigate the effect of near zero $\{\lambda_i\}$ on the variance of \hat{x}_{BP} . A common regularized inversion is diagonal loading: inverting $\mathbf{A}\mathbf{A}^T + \epsilon\mathbf{I}_n$ instead of $\mathbf{A}\mathbf{A}^T$, where ϵ is a parameter. This is equivalent to replacing λ_i^2 with $\lambda_i^2 + \epsilon$ in the eigen-decomposition of $\mathbf{A}^T\mathbf{A}$.

For \hat{x}_{BP} with such a regularized inversion, it is not hard to repeat the computations in (22) and obtain a very similar result, where $1_{i \leq m}$ is replaced with $\lambda_i^2 / (\lambda_i^2 + \epsilon)$ and $\lambda_i^{-2} 1_{i \leq m}$

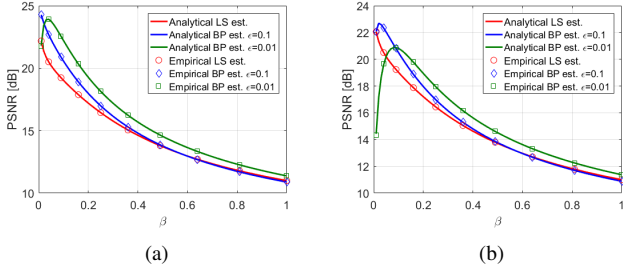


Fig. 6: Deblurring with uniform 9×9 blur kernel, using ℓ_2 prior. PSNR (for *cameraman*) vs. β (regularization parameter), for (a) $\sigma_e = \sqrt{0.3}$, and (b) $\sigma_e = \sqrt{2}$.

is replaced with $\lambda_i^2/(\lambda_i^2 + \epsilon)^2$. Formally, we get

$$\begin{aligned} MSE_{BP} &= \sum_{i=1}^n \left(\frac{\lambda_i^2/(\lambda_i^2 + \epsilon)}{\lambda_i^2/(\lambda_i^2 + \epsilon) + \beta\gamma_i^2} - 1 \right)^2 [\mathbf{V}^T \mathbf{x}]_i^2 \\ &\quad + \sigma_e^2 \sum_{i=1}^n \frac{\lambda_i^2/(\lambda_i^2 + \epsilon)^2}{(\lambda_i^2/(\lambda_i^2 + \epsilon) + \beta\gamma_i^2)^2}, \\ &= \sum_{i=1}^n \left(\frac{\beta\gamma_i^2}{\lambda_i^2/(\lambda_i^2 + \epsilon) + \beta\gamma_i^2} \right)^2 [\mathbf{V}^T \mathbf{x}]_i^2 \\ &\quad + \sigma_e^2 \sum_{i=1}^n \frac{1}{\lambda_i^2(1 + \beta\gamma_i^2(\lambda_i^2 + \epsilon)/\lambda_i^2)^2}. \end{aligned} \quad (25)$$

Therefore, as could be expected, increasing the amount of regularization ϵ reduces the variance of $\hat{\mathbf{x}}_{BP}$ but increases its bias. As a sanity check, observe that for $\epsilon \rightarrow 0$ we get that (25) coincides with (22) (recall $m = n$). Since in this case the performance of $\hat{\mathbf{x}}_{BP}$ depends on the couple (β, ϵ) , we cannot obtain clear properties like Observations 1 and 2 that hold uniformly for any parameter setting. Yet, as demonstrated below and in the sequel, we have empirically observed that it is possible to find settings of (β, ϵ) that balance the bias and variance of $\hat{\mathbf{x}}_{BP}$ and therefore lead to very good results despite the observed noise.

We verify (25) for the uniform blur kernel mentioned above, and two levels of Gaussian noise: $\sigma_e = \sqrt{0.3}$ and $\sigma_e = \sqrt{2}$. The experiments are performed on the 64×64 version of *cameraman* image, and we use again the ℓ_2 prior. The results are presented in Fig. 6. They show that $\hat{\mathbf{x}}_{BP}$ with good tuning of (β, ϵ) can outperform $\hat{\mathbf{x}}_{LS}$, especially when the noise level is low. This implies that "well-tuned" $\hat{\mathbf{x}}_{BP}$ handles the many small singular values of \mathbf{A} (Fig. 1b) better than $\hat{\mathbf{x}}_{LS}$.

V. EXPERIMENTS WITH SOPHISTICATED PRIORS

In this section we empirically demonstrate that the behavior of $\hat{\mathbf{x}}_{BP}$ and $\hat{\mathbf{x}}_{LS}$ (the minimizers of $f_{BP}(\tilde{\mathbf{x}})$ and $f_{LS}(\tilde{\mathbf{x}})$) for sophisticated convex and non-convex priors (for whom mathematical analysis is hard or even intractable) strongly correlates with properties for which we have established concrete mathematical reasoning in the case of ℓ_2 priors. Specifically, we empirically show that using the BP cost function can lead to improved results compared to the LS cost function in super-resolution and deblurring tasks (where the singular values of \mathbf{A} are small), and that there is inverse proportion between the

performance gap and the noise level. On the other hand, the improvement that the BP cost yields is less significant (or may not exist) in certain compressed sensing scenarios (when the singular values of \mathbf{A} are greater than 1).

A. TV prior

We start with the widely-used (isotropic) total-variation (TV) prior [1], which is given by

$$s(\tilde{\mathbf{x}}) = 0.1 \sum_{i,j} \sqrt{|\tilde{x}_{i+1,j} - \tilde{x}_{i,j}|^2 + |\tilde{x}_{i,j+1} - \tilde{x}_{i,j}|^2} \quad (26)$$

for a two-dimensional signal $\tilde{\mathbf{x}}$. The factor 0.1 is used to achieve good performance for $\beta = \sigma_e^2$ in case of denoising ($\mathbf{A} = \mathbf{I}_n$). Obviously, it does not affect the comparison between the methods, since $s(\tilde{\mathbf{x}})$ is multiplied by β that can be set arbitrarily. Note that $s(\tilde{\mathbf{x}})$ is convex, and thus $f_{LS}(\tilde{\mathbf{x}})$ and $f_{BP}(\tilde{\mathbf{x}})$ are also convex functions. We choose to minimize them by the same method: 100 iterations of FISTA [20], which is basically a variant of ISTA (12), incorporating Nesterov's accelerated gradient [45]. The step size μ is the typical 1 over the Lipschitz constant of $\nabla \ell(\tilde{\mathbf{x}})$, i.e. $\mu = 1/\|\mathbf{P}_A\| = 1$ for BP recovery and $\mu = 1/\|\mathbf{A}^T \mathbf{A}\|$ (computed by the power method) for LS recovery. The proximal mapping of $s(\tilde{\mathbf{x}})$ (i.e. Gaussian denoising associated with this prior) is performed using split Bregman method [46]. The experiments are performed on the following eight classical test images: *cameraman*, *house*, *peppers*, *Lena*, *Barbara*, *boat*, *hill* and *couple*.

1) *Super-resolution*: We compare the performance of $\hat{\mathbf{x}}_{LS}$ and $\hat{\mathbf{x}}_{BP}$ for SR with Gaussian anti-aliasing kernel (defined in Section IV-A) and scale factor of 3. We consider the noiseless case $\sigma_e = 0$, as well as the case of Gaussian noise with $\sigma_e = \sqrt{2}$. For both estimators we initialize FISTA with the bicubic upsampling of \mathbf{y} . Fig. 7 shows the PSNR of the reconstructions, averaged over all images, for different values of the regularization parameter β . Fig. 8 shows the average PSNR as a function of the iteration number, where for each estimator we use the value of β which has led to its best results in Fig. 7 (0.25 for LS and 16 for BP in Fig. 8a; 0.5 for LS and 46 for BP in Fig. 8b). It can be seen that $\hat{\mathbf{x}}_{BP}$ converges somewhat faster than $\hat{\mathbf{x}}_{LS}$. In Figs. 15c and 15d we also display the results for *cameraman* image in the noiseless case.

Note the agreement of the obtained results with the observations from Section III, even though they have been established for a much simpler convex prior. In the noiseless case, $\hat{\mathbf{x}}_{BP}$ outperforms $\hat{\mathbf{x}}_{LS}$ for any value of β , while in the noisy scenario, this does not hold. However, even in the latter case, $\hat{\mathbf{x}}_{BP}$ (with good tuning of β) outperforms $\hat{\mathbf{x}}_{LS}$ (with good tuning of β). Yet, the gap between them (for optimal tuning) is smaller than in the noiseless case.

2) *Deblurring*: We compare the two estimators for the widely examined 9×9 uniform blur kernel mentioned in Section IV-C. We make the common assumption of circular shift-invariant blur operator, which allows fast implementation of the gradient steps in the optimization schemes using Fast Fourier Transform (FFT). We consider two levels of Gaussian noise: $\sigma_e = \sqrt{0.3}$ and $\sigma_e = \sqrt{2}$. For both estimators we

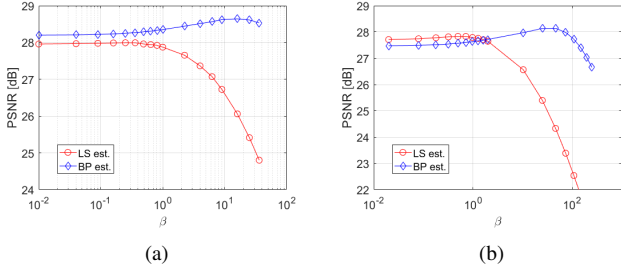


Fig. 7: Super-resolution with Gaussian filter and scale factor of 3, using TV prior and 100 iterations of FISTA. PSNR (averaged over 8 test images) vs. β (regularization parameter), for (a) $\sigma_e = 0$, and (b) $\sigma_e = \sqrt{2}$.

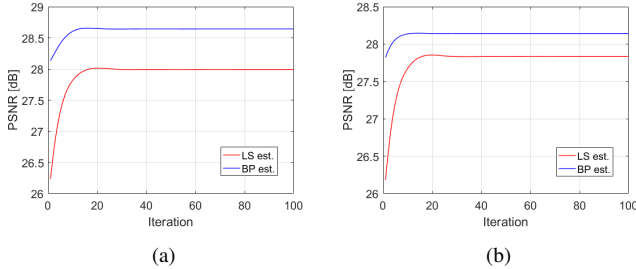


Fig. 8: Super-resolution with Gaussian filter and scale factor of 3, using TV prior. PSNR (for best uniform setting of β , averaged over 8 test images) vs. FISTA iteration number, for (a) $\sigma_e = 0$, and (b) $\sigma_e = \sqrt{2}$.

initialize FISTA with \mathbf{y} , and for $\hat{\mathbf{x}}_{BP}$ we use $\epsilon = 0.01\sigma_e^2$. Fig. 9 shows the average PSNR for different values of β , and Fig. 10 shows the average PSNR as a function of the iteration number, where each estimator uses the best β from Fig. 9 (0.3 for LS and 20.5 for BP in Fig. 10a; 0.98 for LS and 19.5 for BP in Fig. 10b). Note that $\hat{\mathbf{x}}_{BP}$ converges much faster than $\hat{\mathbf{x}}_{LS}$. The difference here for deblurring is more significant than for SR. Visual results for *couple* image in the case of $\sigma_e = \sqrt{2}$ are presented in Figs. 16c and 16d.

The obtained results agree with the observations in Section IV-C, in the sense that there exist settings of (β, ϵ) for which $\hat{\mathbf{x}}_{BP}$ outperforms $\hat{\mathbf{x}}_{LS}$. Presumably, even for the more complex TV prior, this is due to better handling the many near-zero singular values of \mathbf{A} . As expected, the performance gap between the estimators (for optimal tuning) decreases when the noise level is higher. However, it is still highly in favor of $\hat{\mathbf{x}}_{BP}$.

B. BM3D prior

We turn to compare the performance of the two cost functions for the BM3D prior [4], which is based on sparsifying a three-dimensional transformation applied to groups of nearest-neighbor (i.e. similar) patches. This prior is non-convex. In fact, it is also not clear how to precisely formulate its associated $s(\tilde{\mathbf{x}})$. Yet, the proximal mapping of $s(\tilde{\mathbf{x}})$ can be performed by applying the BM3D denoiser as a “black-box”. We use 200 iterations of FISTA to minimize the cost functions with typical step sizes as explained above, and the same eight classical test images.

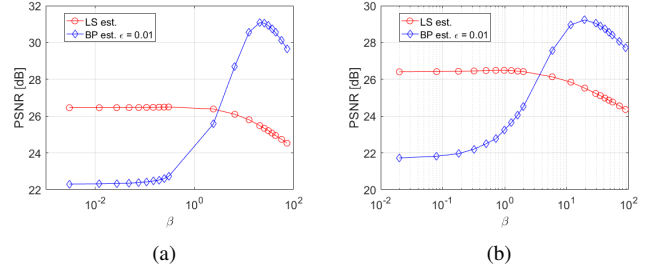


Fig. 9: Deblurring with uniform 9×9 blur kernel, using TV prior and 100 iterations of FISTA. PSNR (averaged over 8 test images) vs. β (regularization parameter), for (a) $\sigma_e = \sqrt{0.3}$, and (b) $\sigma_e = \sqrt{2}$.

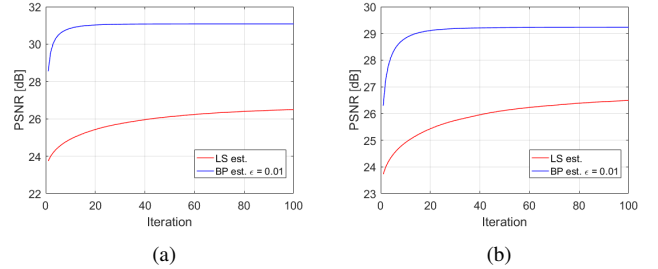


Fig. 10: Deblurring with uniform 9×9 blur kernel, using TV prior. PSNR (for best uniform setting of β , averaged over 8 test images) vs. FISTA iteration number, for (a) $\sigma_e = \sqrt{0.3}$, and (b) $\sigma_e = \sqrt{2}$.

1) *Super-resolution*: We repeat the two SR experiments of Section V-A1. Fig. 11 shows the average PSNR for different values of β , and Fig. 12 shows the average PSNR as a function of the iteration number, where each estimator uses the best β from Fig. 11 (0.09 for LS and 16 for BP in Fig. 12a; 0.5 for LS and 140 for BP in Fig. 12b). Again, note that $\hat{\mathbf{x}}_{BP}$ converges much faster than $\hat{\mathbf{x}}_{LS}$. In Figs. 15e and 15f we display the results for *cameraman* image in the noiseless case.

Note the strong correlation between the obtained results and the observations from Section III, even though the prior is highly non-convex. In the noiseless case, $\hat{\mathbf{x}}_{BP}$ outperforms $\hat{\mathbf{x}}_{LS}$ for a large range of β . For very small values of β it is inferior to $\hat{\mathbf{x}}_{LS}$, but with only a small gap. From a practitioner point of view, the advantages of using the BP cost here are still clear, since when β is well-tuned (for each of the cost functions) $\hat{\mathbf{x}}_{BP}$ is significantly better. Note that in the examined noisy scenario, well-tuned $\hat{\mathbf{x}}_{BP}$ is still better than well-tuned $\hat{\mathbf{x}}_{LS}$, but the gap decreases.

2) *Deblurring*: We repeat the two deblurring experiments of Section V-A2. Fig. 13 shows the average PSNR for different values of β , and Fig. 14 shows the average PSNR as a function of the iteration number, where each estimator uses the best β from Fig. 13 (0.027 for LS and 25.5 for BP in Fig. 14a; 0.5 for LS and 29.5 for BP in Fig. 14b). Figs. 16e and 16f present visual results for *couple* image in the case of $\sigma_e = \sqrt{2}$. The observations that have been made for TV prior stay the same here for the BM3D prior: There exist settings of (β, ϵ) for which $\hat{\mathbf{x}}_{BP}$ significantly outperforms $\hat{\mathbf{x}}_{LS}$ and converges faster.

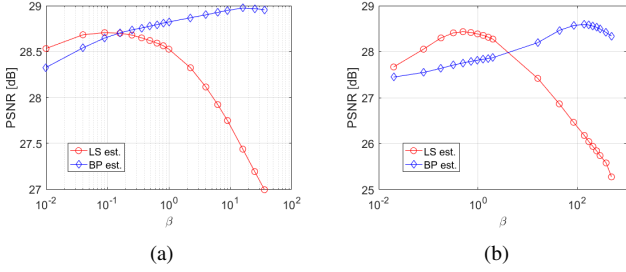


Fig. 11: Super-resolution with Gaussian filter and scale factor of 3, using BM3D prior and 200 iterations of FISTA. PSNR (averaged over 8 test images) vs. β (regularization parameter), for (a) $\sigma_e = 0$, and (b) $\sigma_e = \sqrt{2}$.

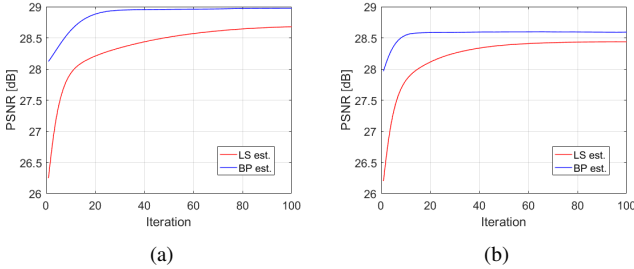


Fig. 12: Super-resolution with Gaussian filter and scale factor of 3, using BM3D prior. PSNR (for best uniform setting of β , averaged over 8 test images) vs. FISTA iteration number, for (a) $\sigma_e = 0$, and (b) $\sigma_e = \sqrt{2}$.

C. DCGAN prior

The developments in deep learning [47] in the recent years have led to significant improvement in learning generative models. Methods like variational auto-encoders (VAEs) [48] and generative adversarial networks (GANs) [49] have found success at modeling data distributions. This has naturally led to using pre-trained generative models as priors in imaging inverse problems [17]. Since in popular generative models [48], [49] a generator $\mathcal{G}(\cdot)$ learns a mapping from a low dimensional space $z \in \mathbb{R}^d$ to the signal space $\mathcal{G}(z) \in \mathbb{R}^n$, one can search for a reconstruction of x only in the range of the generator. This can be formulated by the following non-convex prior

$$s(\tilde{x}) = \begin{cases} 0, & \exists \tilde{z} \in \mathbb{R}^d : \tilde{x} = \mathcal{G}(\tilde{z}) \\ +\infty, & \text{otherwise} \end{cases}. \quad (27)$$

Plugging (27) into the typical cost function (5), we get the objective

$$f_{LS}(\tilde{z}) = \|\mathbf{y} - \mathbf{A}\mathcal{G}(\tilde{z})\|_2^2. \quad (28)$$

Note that for this prior, a regularization parameter β is not required. The recovery of the latent image x is given by $\hat{x}_{LS} = \mathcal{G}(\hat{z}_{LS})$, where \hat{z}_{LS} is a minimizer of (28), which can be obtained by backpropagation and standard gradient based optimizers.

The technique above has been examined recently in [17]. Here, we compare it with the one obtained by a similar

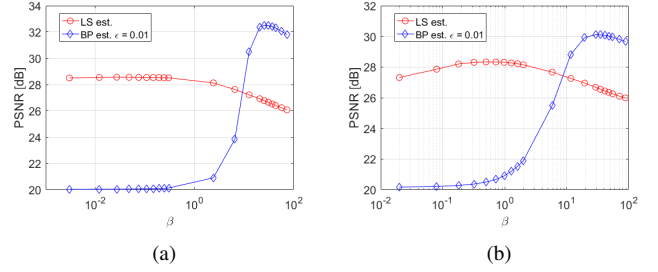


Fig. 13: Deblurring with uniform 9×9 blur kernel, using BM3D prior and 200 iterations of FISTA. PSNR (averaged over 8 test images) vs. β (regularization parameter), for (a) $\sigma_e = \sqrt{0.3}$, and (b) $\sigma_e = \sqrt{2}$.

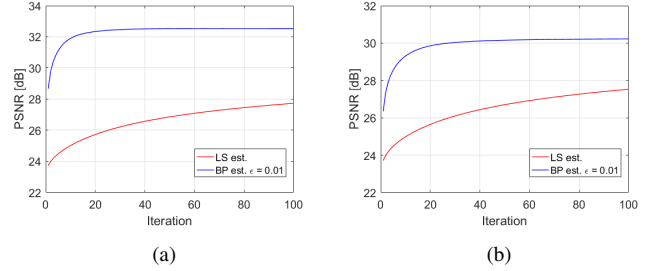


Fig. 14: Deblurring with uniform 9×9 blur kernel, using BM3D prior. PSNR (for best uniform setting of β , averaged over 8 test images) vs. FISTA iteration number, for (a) $\sigma_e = \sqrt{0.3}$, and (b) $\sigma_e = \sqrt{2}$.

approach that uses the BP cost function (6), i.e. we plug (27) into (6), to get the objective

$$f_{BP}(\tilde{z}) = \|\mathbf{A}^\dagger(\mathbf{y} - \mathbf{A}\mathcal{G}(\tilde{z}))\|_2^2, \quad (29)$$

and recover x by $\hat{x}_{BP} = \mathcal{G}(\hat{z}_{BP})$, where \hat{z}_{BP} is a minimizer of (29).

We use the CelebA dataset [50] and Tensorflow package [51] to train a generator using DCGAN architecture [19] on the cropped version of the images (64×64 pixels), as done in [17]. We use the first 200,000 images (out of 202,599) for training, and the training procedure follows the one in [17], [19]. At test time, all the optimizations with respect to z are performed using: ADAM [21] with learning rate of 0.1 (as done in [17]), same 10 random initializations of z , and 2000 iterations, which suffice for ensuring that the objectives (28) and (29) stop decreasing. The value of z that gives the lowest objective is chosen.

1) *Super-resolution*: We compare the performance of \hat{x}_{LS} and \hat{x}_{BP} for SR with Gaussian anti-aliasing kernel (defined in Section IV-A) and scale factor of 3. Table I shows the PSNR results for the different cost functions, averaged over the last 20 images in CelebA (these images are not included in the training data). Several visual results are shown in Fig. 17.

It can be seen that the BP fidelity yields higher average PSNR and perceptually better recoveries. In fact, in each of the 20 examined images \hat{x}_{BP} has obtained higher PSNR than \hat{x}_{LS} . This behavior agrees with the previous experiments that demonstrate the advantages of the BP cost for the noiseless SR problem. We also note that even though the results of the simple bicubic upsampling are always perceptually worse than the recoveries that use DCGAN, its PSNR is sometimes



(a) Original image

(b) Bicubic (22.83 dB)



(c) LS-TV (24.37 dB)

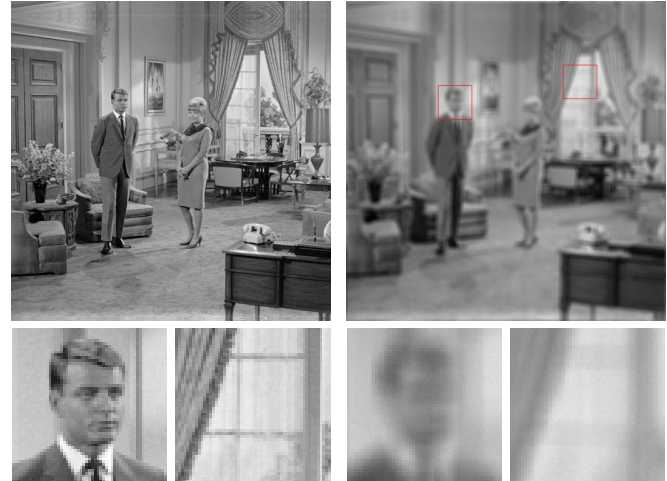
(d) BP-TV (24.94 dB)



(e) LS-BM3D (25.02 dB)

(f) BP-BM3D (25.38 dB)

Fig. 15: Super-resolution with Gaussian filter, scale factor of 3 and $\sigma_e = 0$ for *cameraman* image. From left to right and from top to bottom: original image, bicubic upsampling, reconstruction of LS fidelity with TV prior, reconstruction of BP fidelity with TV prior, reconstruction of LS fidelity with BM3D prior, and reconstruction of BP fidelity with BM3D prior.



(a) Original image

(b) Blurred and noisy image



(c) LS-TV (26.45 dB)

(d) BP-TV (29.28 dB)



(e) LS-BM3D (28.74 dB)

(f) BP-BM3D (30.38 dB)

Fig. 16: Deblurring with uniform 9×9 blur kernel and $\sigma_e = \sqrt{2}$ for *couple* image. From left to right and from top to bottom: original image, blurred and noisy image, reconstruction of LS fidelity with TV prior, reconstruction of BP fidelity with TV prior, reconstruction of LS fidelity with BM3D prior, and reconstruction of BP fidelity with BM3D prior.

TABLE I: Reconstruction PSNR [dB] (averaged over 20 images from CelebA) for super-resolution with Gaussian filter and scale factor of 3, using DCGAN prior and ADAM optimizer.

	Bicubic	LS est.	BP est.
SR x3	22.55	22.73	23.45

TABLE II: Reconstruction PSNR [dB] (averaged over 20 images from CelebA) for compressed sensing with Gaussian measurement matrix, using DCGAN prior and ADAM optimizer.

	Naive $\mathbf{A}^\dagger \mathbf{y}$	LS est.	BP est.
CS $m/n = 0.1$	12.24	22.56	22.51
CS $m/n = 0.5$	14.85	23.43	23.60

higher. This drawback of GAN-based priors is due to the limited representation capabilities of the generators (sometimes referred to as "mode collapse"). A very recent work has suggested to mitigate this deficiency by image-adaptation and back-projections [52].

2) *Compressed sensing*: Due to the small image dimensions, we are able to compare the performance of $\hat{\mathbf{x}}_{BP}$ and $\hat{\mathbf{x}}_{LS}$ for CS with Gaussian measurement matrix (i.e. $A_{ij} \sim \mathcal{N}(0, 1/m)$), for which the two cost functions differ (see the discussion in Section IV-B). We use compression ratios of $m/n = 0.1$ and $m/n = 0.5$. Table II shows the PSNR results for the different cost functions, averaged over the last 20 images in CelebA. Several visual results are shown in Figs. 18 and 19.

The results of $\hat{\mathbf{x}}_{BP}$ are slightly inferior to those of $\hat{\mathbf{x}}_{LS}$ for $m = 0.1n$, and are slightly better for $m = 0.5n$. Note that the improvement (with respect to BP) in the gap between BP and LS in the two scenarios strongly correlates with the analysis in Section III, which explains such behavior for ℓ_2 priors by the fact that for $m = 0.1n$ all the singular values of \mathbf{A} are larger than 1, while for $m = 0.5n$ some of them are smaller than 1. Yet, the fact that the BP cost is only slightly worse than the LS cost for $m = 0.1n$ may hint that it has an additional advantage. Exploring whether such an advantage comes from optimization considerations (similar to the behavior shown in Section IV for ℓ_2 prior and conjugate gradients) is an interesting direction for future research.

VI. CONCLUSION

In this work we examined the BP fidelity term for ill-posed linear inverse problems. This term has only been used implicitly by the recently proposed iterative denoising and backward projections (IDBP) framework, and is an alternative to the least squares (LS) term, which is the common choice in most works. We showed that IDBP is essentially a specific optimization scheme, namely the proximal gradient method (known also as ISTA), for minimizing the cost function induced by the BP fidelity term. Then, we analytically compared the two fidelity terms—BP and LS—for the case of ℓ_2 -type prior functions, and obtained mathematically-backed observations in favor of the BP term when the singular values of the linear operator \mathbf{A} are smaller than 1 and the noise level is moderate (both conditions are satisfied in many applications, such as super-

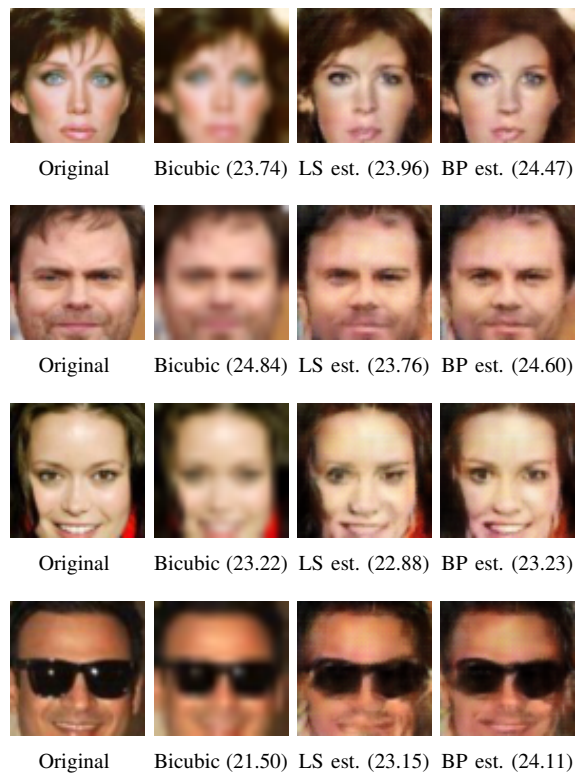


Fig. 17: Super-resolution with Gaussian filter and scale factor of 3, using DCGAN prior.

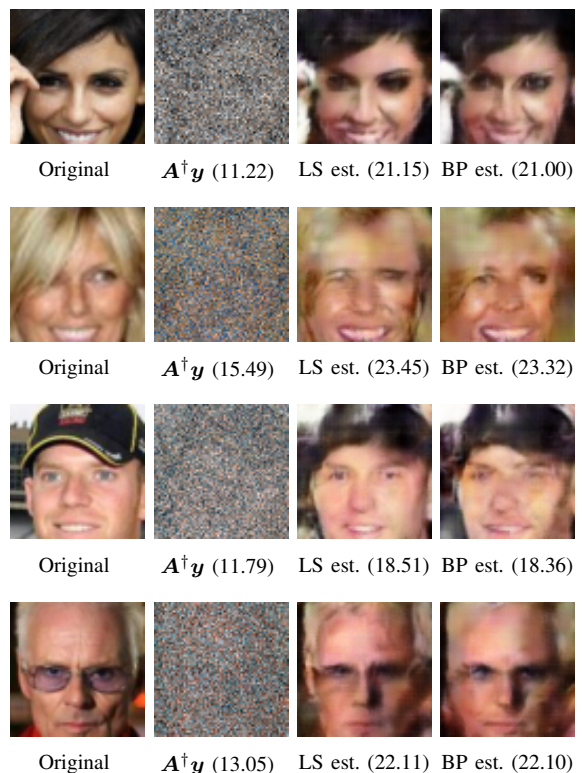


Fig. 18: Compressed sensing with $m = 0.1n$ Gaussian measurements, using DCGAN prior.

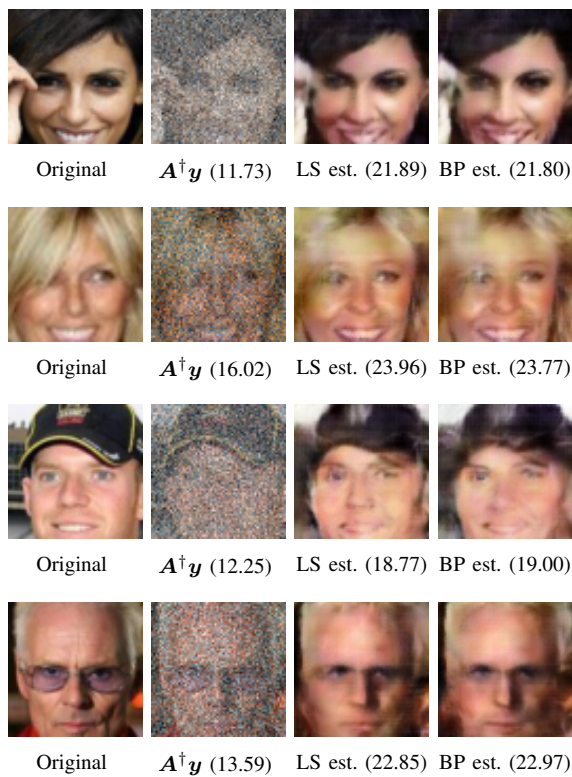


Fig. 19: Compressed sensing with $m = 0.5n$ Gaussian measurements, using DCGAN prior.

resolution and deblurring). Finally, we empirically demonstrated that the behavior for sophisticated priors, such as TV, BM3D and DCGAN, strongly correlates with the theoretically backed properties that we established for ℓ_2 priors. While the mathematical performance analysis in this work is done only for ℓ_2 priors, it provides a good characterization for the advantages of BP and LS compared to each other. Yet, we believe that there are other factors that should be explored with respect to the new fidelity term, such as its behavior with non-convex priors or its effect on the convergence speed of iterative optimization algorithms.

REFERENCES

- [1] L. I. Rudin, S. Osher, and E. Fatemi, "Nonlinear total variation based noise removal algorithms," *Physica D: nonlinear phenomena*, vol. 60, no. 1-4, pp. 259–268, 1992.
- [2] A. Buades, B. Coll, and J.-M. Morel, "A review of image denoising algorithms, with a new one," *Multiscale Modeling & Simulation*, vol. 4, no. 2, pp. 490–530, 2005.
- [3] M. Elad and M. Aharon, "Image denoising via sparse and redundant representations over learned dictionaries," *IEEE Transactions on Image Processing*, vol. 15, no. 12, pp. 3736–3745, 2006.
- [4] K. Dabov, A. Foi, V. Katkovnik, and K. Egiazarian, "Image denoising by sparse 3-D transform-domain collaborative filtering," *IEEE Transactions on image processing*, vol. 16, no. 8, pp. 2080–2095, 2007.
- [5] M. Bertalmio, G. Sapiro, V. Caselles, and C. Ballester, "Image inpainting," in *Proceedings of the 27th annual conference on Computer graphics and interactive techniques*, pp. 417–424, ACM Press/Addison-Wesley Publishing Co., 2000.
- [6] A. Criminisi, P. Pérez, and K. Toyama, "Region filling and object removal by exemplar-based image inpainting," *IEEE Transactions on image processing*, vol. 13, no. 9, pp. 1200–1212, 2004.
- [7] M. Elad, J.-L. Starck, P. Querre, and D. L. Donoho, "Simultaneous cartoon and texture image inpainting using morphological component analysis (MCA)," *Applied and Computational Harmonic Analysis*, vol. 19, no. 3, pp. 340–358, 2005.
- [8] J. A. Guerrero-Colón, L. Mancera, and J. Portilla, "Image restoration using space-variant Gaussian scale mixtures in overcomplete pyramids," *IEEE Transactions on Image Processing*, vol. 17, no. 1, pp. 27–41, 2008.
- [9] A. Danielyan, V. Katkovnik, and K. Egiazarian, "BM3D frames and variational image deblurring," *IEEE Transactions on Image Processing*, vol. 21, no. 4, pp. 1715–1728, 2012.
- [10] J. Yang, J. Wright, T. S. Huang, and Y. Ma, "Image super-resolution via sparse representation," *IEEE transactions on image processing*, vol. 19, no. 11, pp. 2861–2873, 2010.
- [11] W. Dong, L. Zhang, G. Shi, and X. Li, "Nonlocally centralized sparse representation for image restoration," *IEEE Transactions on Image Processing*, vol. 22, no. 4, pp. 1620–1630, 2013.
- [12] D. L. Donoho, "Compressed sensing," *IEEE Transactions on information theory*, vol. 52, no. 4, pp. 1289–1306, 2006.
- [13] M. F. Duarte, M. A. Davenport, D. Takhar, J. N. Laska, T. Sun, K. E. Kelly, R. G. Baraniuk, et al., "Single-pixel imaging via compressive sampling," *IEEE Signal Processing Magazine*, vol. 25, no. 2, p. 83, 2008.
- [14] E. J. Candès and M. B. Wakin, "An introduction to compressive sampling," *IEEE signal processing magazine*, vol. 25, no. 2, pp. 21–30, 2008.
- [15] T. Blumensath, "Sampling and reconstructing signals from a union of linear subspaces," *IEEE Transactions on Information Theory*, vol. 57, no. 7, pp. 4660–4671, 2011.
- [16] T. Tirer and R. Giryès, "Generalizing CoSaMP to signals from a union of low dimensional linear subspaces," *Applied and Computational Harmonic Analysis*, 2018.
- [17] A. Bora, A. Jalal, E. Price, and A. G. Dimakis, "Compressed sensing using generative models," in *Proceedings of the 34th International Conference on Machine Learning-Volume 70*, pp. 537–546, JMLR. org, 2017.
- [18] T. Tirer and R. Giryès, "Image restoration by iterative denoising and backward projections," *IEEE Transactions on Image Processing*, vol. 28, no. 3, pp. 1220–1234, 2019.
- [19] A. Radford, L. Metz, and S. Chintala, "Unsupervised representation learning with deep convolutional generative adversarial networks," *arXiv preprint arXiv:1511.06434*, 2015.
- [20] A. Beck and M. Teboulle, "A fast iterative shrinkage-thresholding algorithm for linear inverse problems," *SIAM journal on imaging sciences*, vol. 2, no. 1, pp. 183–202, 2009.
- [21] D. P. Kingma and J. Ba, "Adam: A method for stochastic optimization," *arXiv preprint arXiv:1412.6980*, 2014.
- [22] P. L. Combettes and J.-C. Pesquet, "Proximal splitting methods in signal processing," in *Fixed-point algorithms for inverse problems in science and engineering*, pp. 185–212, Springer, 2011.
- [23] S. V. Venkatakrishnan, C. A. Bouman, and B. Wohlberg, "Plug-and-play priors for model based reconstruction," in *Global Conference on Signal and Information Processing (GlobalSIP), 2013 IEEE*, pp. 945–948, IEEE, 2013.
- [24] S. Sreehari, S. V. Venkatakrishnan, B. Wohlberg, G. T. Buzzard, L. F. Drummy, J. P. Simmons, and C. A. Bouman, "Plug-and-play priors for bright field electron tomography and sparse interpolation," *IEEE Transactions on Computational Imaging*, vol. 2, no. 4, pp. 408–423, 2016.
- [25] Y. Romano, M. Elad, and P. Milanfar, "The little engine that could: Regularization by denoising (RED)," *SIAM Journal on Imaging Sciences*, vol. 10, no. 4, pp. 1804–1844, 2017.
- [26] A. M. Teodoro, J. M. Bioucas-Dias, and M. A. Figueiredo, "Image restoration and reconstruction using variable splitting and class-adapted image priors," in *Image Processing (ICIP), 2016 IEEE International Conference on*, pp. 3518–3522, IEEE, 2016.
- [27] U. S. Kamilov, H. Mansour, and B. Wohlberg, "A plug-and-play priors approach for solving nonlinear imaging inverse problems," *IEEE Signal Processing Letters*, vol. 24, no. 12, pp. 1872–1876, 2017.
- [28] S. H. Chan, X. Wang, and O. A. Elgendy, "Plug-and-play ADMM for image restoration: Fixed-point convergence and applications," *IEEE Transactions on Computational Imaging*, vol. 3, no. 1, pp. 84–98, 2017.
- [29] K. Zhang, W. Zuo, S. Gu, and L. Zhang, "Learning deep CNN denoiser prior for image restoration," in *Proceedings of the IEEE Conference on Computer Vision and Pattern Recognition*, pp. 3929–3938, 2017.
- [30] Y. Sun, B. Wohlberg, and U. S. Kamilov, "An online plug-and-play algorithm for regularized image reconstruction," *IEEE Transactions on Computational Imaging*, 2019.

- [31] S. Ono, "Primal-dual plug-and-play image restoration," *IEEE Signal Processing Letters*, vol. 24, no. 8, pp. 1108–1112, 2017.
- [32] S. Boyd, N. Parikh, E. Chu, B. Peleato, and J. Eckstein, "Distributed optimization and statistical learning via the alternating direction method of multipliers," *Foundations and Trends® in Machine Learning*, vol. 3, no. 1, pp. 1–122, 2011.
- [33] J. Nocedal and S. J. Wright, *Numerical Optimization*. Springer, 2006.
- [34] M. R. Hestenes and E. Stiefel, *Methods of conjugate gradients for solving linear systems*, vol. 49. 1952.
- [35] T. Tirer and R. Giryes, "An iterative denoising and backwards projections method and its advantages for blind deblurring," in *2018 25th IEEE International Conference on Image Processing (ICIP)*, pp. 973–977, IEEE, 2018.
- [36] T. Tirer and R. Giryes, "Super-resolution via image-adapted denoising CNNs: Incorporating external and internal learning," *IEEE Signal Processing Letters*, vol. 26, no. 7, pp. 1080–1084, 2019.
- [37] I. Daubechies, M. Defrise, and C. De Mol, "An iterative thresholding algorithm for linear inverse problems with a sparsity constraint," *Communications on Pure and Applied Mathematics: A Journal Issued by the Courant Institute of Mathematical Sciences*, vol. 57, no. 11, pp. 1413–1457, 2004.
- [38] J.-J. Moreau, "Proximité et dualité dans un espace hilbertien," *Bull. Soc. Math. France*, vol. 93, no. 2, pp. 273–299, 1965.
- [39] R. A. Horn and C. R. Johnson, *Matrix analysis*. Cambridge university press, 2012.
- [40] E. T. Hale, W. Yin, and Y. Zhang, "Fixed-point continuation for ℓ_1 -minimization: Methodology and convergence," *SIAM Journal on Optimization*, vol. 19, no. 3, pp. 1107–1130, 2008.
- [41] R. Giryes, Y. C. Eldar, A. M. Bronstein, and G. Sapiro, "Tradeoffs between convergence speed and reconstruction accuracy in inverse problems," *IEEE Transactions on Signal Processing*, vol. 66, no. 7, pp. 1676–1690, 2018.
- [42] C. T. Kelley, *Iterative methods for linear and nonlinear equations*, vol. 16. Siam, 1995.
- [43] M. Lustig, D. Donoho, and J. M. Pauly, "Sparse MRI: The application of compressed sensing for rapid mr imaging," *Magnetic Resonance in Medicine: An Official Journal of the International Society for Magnetic Resonance in Medicine*, vol. 58, no. 6, pp. 1182–1195, 2007.
- [44] J. Kovacevic, A. Chebira, *et al.*, "An introduction to frames," *Foundations and Trends® in Signal Processing*, vol. 2, no. 1, pp. 1–94, 2008.
- [45] Y. E. Nesterov, "A method for solving the convex programming problem with convergence rate $\mathcal{O}(1/k^2)$," in *Dokl. akad. nauk Sssr*, vol. 269, pp. 543–547, 1983.
- [46] T. Goldstein and S. Osher, "The split Bregman method for L1-regularized problems," *SIAM journal on imaging sciences*, vol. 2, no. 2, pp. 323–343, 2009.
- [47] I. Goodfellow, Y. Bengio, and A. Courville, *Deep learning*. 2016.
- [48] D. P. Kingma and M. Welling, "Auto-encoding variational bayes," *arXiv preprint arXiv:1312.6114*, 2013.
- [49] I. Goodfellow, J. Pouget-Abadie, M. Mirza, B. Xu, D. Warde-Farley, S. Ozair, A. Courville, and Y. Bengio, "Generative adversarial nets," in *Advances in neural information processing systems*, pp. 2672–2680, 2014.
- [50] Z. Liu, P. Luo, X. Wang, and X. Tang, "Deep learning face attributes in the wild," in *Proceedings of the IEEE international conference on computer vision*, pp. 3730–3738, 2015.
- [51] M. Abadi, P. Barham, J. Chen, Z. Chen, A. Davis, J. Dean, M. Devin, S. Ghemawat, G. Irving, M. Isard, *et al.*, "Tensorflow: A system for large-scale machine learning," in *12th {USENIX} Symposium on Operating Systems Design and Implementation ({OSDI} 16)*, pp. 265–283, 2016.
- [52] S. Abu Hussein, T. Tirer, and R. Giryes, "Image-adaptive GAN based reconstruction," *arXiv preprint arXiv:1906.05284*, 2019.